DRAFT VERSION NOVEMBER 6, 2015
Preprint typeset using LaTeX style emulateapj v. 03/07/07

arXiv:1510.03153v2 [astro-ph.HE] 5 Nov 2015

[O III]λ5007 AND X-RAY PROPERTIES OF A COMPLETE SAMPLE OF HARD X-RAY SELECTED AGNS IN THE LOCAL UNIVERSE

Y. UEDA[1], Y. HASHIMOTO[2], K. ICHIKAWA[1,3], Y. ISHINO[1], A.Y. KNIAZEV[4,5,6], P. VÄISÄNEN[4,5], C. RICCI[1,7,8], S. BERNEY[9], P. GANDHI[10], M. KOSS[9], R. MUSHOTZKY[11], Y. TERASHIMA[12], B. TRAKHTENBROT[9], M. CRENSHAW[13]

Draft version November 6, 2015

ABSTRACT

We study the correlation between the [O III]λ5007 and X-ray luminosities of local Active Galactic Nuclei (AGNs), using a complete, hard X-ray (>10 keV) selected sample in the Swift/BAT 9-month catalog. From our optical spectroscopic observations at the South African Astronomical Observatory and the literature, a catalog of [O III]λ5007 line flux for all 103 AGNs at Galactic latitudes of $|b|>15^\circ$ is complied. Significant correlations with intrinsic X-ray luminosity ($L_{\rm X}$) are found both for observed ($L_{\rm [O\ III]}$) and extinction-corrected ($L^{\rm cor}_{\rm [O\ III]}$) luminosities, separately for X-ray unabsorbed and absorbed AGNs. We obtain the regression form of $L_{\rm [O\ III]} \propto L_{\rm 2-10\ keV}^{1.18\pm0.07}$ and $L^{\rm cor}_{\rm [O\ III]} \propto L_{\rm 2-10\ keV}^{1.16\pm0.09}$ from the whole sample. The absorbed AGNs with low ($<0.5\%$) scattering fractions in soft X-rays show on average smaller $L_{\rm [O\ III]}/L_{\rm X}$ and $L^{\rm cor}_{\rm [O\ III]}/L_{\rm X}$ ratios than the other absorbed AGNs, while those in edge-on host galaxies do not. These results suggest that a significant fraction of this population are buried in tori with small opening angles. By using these $L_{\rm [O\ III]}$ vs. $L_{\rm X}$ correlations, the X-ray luminosity function of local AGNs (including Compton thick AGNs) in a standard population synthesis model gives much better agreement with the [O III]λ5007 luminosity function derived from the Sloan Digital Sky Survey than previously reported. This confirms that hard X-ray observations are a very powerful tool to find AGNs with high completeness.

Subject headings: galaxies: active — galaxies: Seyfert — quasars: general — X-rays: galaxies

1. INTRODUCTION

In order to reveal the growth history of supermassive black holes (SMBHs) in galactic centers, it is crucial to completely survey all types of active galactic nuclei (AGNs) in the universe. According to the unified scheme of AGNs (Antonucci 1993), an SMBH is surrounded by a bagel-shaped, dusty torus and only the viewing angle determines the observable nature of an AGN; one sees type-1 and type-2 AGNs when the line of sight is unblocked and blocked by the torus, respectively, which causes dust extinction of optical lights from the accretion disk and broad line region (BLR) and photoelectric absorption (plus Compton scattering) of the primary X-ray emission. Basically, the unified scheme seems fairly successful to explain many aspects of AGN phenomena. The spectrum of the X-ray background indicates that a dominant population of AGNs are type-2 (obscured) AGNs (e.g., Ueda et al. 2014). Hence, surveys only using the broad emission lines or soft X-rays could easily miss the main population of AGNs.

Emission lines from the narrow-line region (NLR), which is located outside the inner torus region, should be observable both from type-1 and type-2 AGNs unless the SMBH is entirely surrounded by the torus. Thus, as long as the unified scheme holds, narrow emission lines induced by an AGN, such as [O III]λ5007, have been considered to be a useful indicator of the AGN luminosity, even in Compton-thick AGNs whose "observed" X-ray flux below 10 keV is significantly attenuated (e.g., LaMassa et al. 2009). If, however, there is a wide scatter between the line luminosity and the intrinsic AGN luminosity, surveys based on the narrow lines may be subject to strong selection effects. Also, optical and ultraviolet lines are very sensitive to extinction by interstellar dust in the host galaxy and by circumnuclear dust that may be present around the NLR. Note that contamination from star-forming activities in the host galaxy may become a problem to make a clean AGN sample based on the [O III]λ5007 flux (Simpson 2005; Toba et al. 2014).

Hard X-ray observations at rest-frame energies above 10 keV are able to provide the least biased AGN samples against obscuration thanks to their strong penetrating power, except for heavily Compton-thick AGNs with column densities of $\log N_{\rm H} \gtrsim 25$ (Tueller et al. 2008). From these surveys, AGNs with very low scattering fractions in soft X-rays have been discovered (Ueda et al. 2007), many of which were missed in previous optical surveys because of their weak [O III]λ5007 emission. It has been suspected that the AGNs might be buried in very geometrically-thick tori, although Hönig et al. (2014) suggest that a part of them may be subject to interstellar absorption by the host galaxy. In geometrically-thick tori with small opening angles, the AGN should have fainter intrinsic [O III]λ5007 luminosity relative to the hard X-ray

[1] Department of Astronomy, Kyoto University, Kyoto 606-8502, Japan
[2] Department of Earth Sciences, National Taiwan Normal University, No. 88, Sec. 4, Tingzhou Rd., Wenshan District, Taipei 11677, Taiwan R.O.C
[3] National Astronomical Observatory, 2-21-1 Osawa, Mitaka, Tokyo 181-8588, Japan
[4] South African Astronomical Observatory, PO Box 9, 7935 Observatory, Cape Town, South Africa
[5] Southern African Large Telescope Foundation, PO Box 9, 7935 Observatory, Cape Town, South Africa
[6] Sternberg Astronomical Institute, Lomonosov Moscow State University, Moscow, Russia
[7] Pontificia Universidad Catolica de Chile, Instituto de Astrofisica, Casilla 306, Santiago 22, Chile
[8] EMBIGGEN Anillo, Concepcion, Chile
[9] Department of Physics, Institute for Astronomy, ETH Zurich, Wolfgang-Pauli-Strasse 27, CH-8093 Zurich, Switzerland
[10] School of Physics & Astronomy, University of Southampton, Highfield, Southampton SO17 1BJ, UK
[11] Department of Astronomy, University of Maryland, College Park, MD 20742-2421, USA
[12] Department of Physics, Ehime University, Matsuyama 790-8577, Japan
[13] Department of Physics and Astronomy, Georgia State University, 25 Park Place, Suite 605, Atlanta, GA 30303, USA

luminosity compared with classical Seyfert 2 galaxies, because much less of the nuclear flux leaks out to ionize the NLR. An extreme case can be found in ultra luminous infrared galaxies (ULIRGs) that contain buried AGNs almost entirely surrounded by Compton-thick matter (Imanishi et al. 2007; Ichikawa et al. 2014).

Thus, AGN selections using [O III]λ5007 line and hard X-rays are considered to be complementary to each other in detecting obscured populations. It is therefore very important to study the correlations between [O III]λ5007 and hard X-ray luminosities so that we can compare the statistical quantities of AGNs (such as luminosity function) obtained from these different surveys, and evaluate the completeness and cleanness of each selection. For this study, we need to use a statistically complete sample of all types of AGNs with well known properties.

Following early works by Mulchaey et al. (1994) for Seyfert 1s and 2s and by Polletta et al. (1996) and Alonso-Herrero et al. (1997) for Seyfert 2s, several authors have studied correlations between [O III]λ5007 and hard X-ray luminosities, using various samples of local AGNs (e.g., Heckman et al. 2005; Panessa et al. 2006; Netzer et al. 2006; Meléndez et al. 2008; Lamastra et al. 2009). Heckman et al. (2005) and Meléndez et al. (2008) use observed [O III]λ5007 luminosities (hereafter $L_{[\mathrm{O\ III}]}$), while the others use those corrected for extinction (hereafter $L^{\mathrm{cor}}_{[\mathrm{O\ III}]}$). Among these works, only Meléndez et al. (2008), who have more focus on the [O IV] 25.89μm line, use an AGN sample based on hard X-ray surveys above 10 keV, although the sample is not statistically complete and is limited in number (40). The quantitative results of the [O III]λ5007 and X-ray luminosity correlation obtained so far have been a little puzzling. From combined samples of type-1 and type-2 AGNs, Panessa et al. (2006) obtained a regression of the form $L^{\mathrm{cor}}_{[\mathrm{O\ III}]} \propto L_{\mathrm{X}}^{0.82\pm0.04}$, whereas Lamastra et al. (2009) found an almost linear correlation of $L^{\mathrm{cor}}_{[\mathrm{O\ III}]} \propto L_{\mathrm{X}}^{0.98\pm0.06}$.

In this paper, we investigate the correlation between the [O III]λ5007 and X-ray luminosities, using a *complete* sample consisting of 103 objects at Galactic latitudes of $|b| > 15^\circ$ in the Swift/BAT 9-month hard X-ray survey (Tueller et al. 2008). To follow-up sources in the southern hemisphere, many of which did not have optical spectra, we conducted systematic optical spectroscopic observations at the SAAO. Then we complement it with a compilation from the literature, including Winter et al. (2010a), where the optical spectra of Swift/BAT 9-month AGNs in the northern sky are analyzed. Section 2 describes the sample, optical observations and data reduction, and present the catalog of the [O III]λ5007 flux together with those of narrow Hα and Hβ lines whenever available. In Section 3, we present the results of correlation analysis between the [O III]λ5007 (or narrow Hα) luminosity and intrinsic (de-absorbed) X-ray luminosity for different types of AGNs. We then discuss the origin of these correlations, and compare [O III]λ5007, Hα, and X-ray luminosity functions of local AGNs in Section 4. The conclusions are summarized in Section 5. Throughout the paper, we adopt $H_0 = 70$ km s^{-1} Mpc^{-1}, $\Omega_{\mathrm{M}} = 0.3$, and $\Omega_\Lambda = 0.7$.

2. THE OPTICAL SPECTROSCOPY DATA

2.1. *Parent Sample*

For our study, we utilize the Swift/BAT 9 month catalog (Tueller et al. 2008) to define a complete sample of hard X-ray selected AGNs in the local universe. The Tueller et al. (2008) catalog contains 137 AGNs in total excluding blazars at a flux limit of 2×10^{-11} erg cm^{-2} s^{-1} in the 14–195 keV band with detection significance above 4.8σ. To minimize the effects of extinction by Galactic interstellar medium, we limit the sample to those located at high Galactic latitudes of $|b| > 15^\circ$ for our optical spectral studies. We exclude Cen A, which is a very nearby object, and SWIFT J0350.1–5019, which likely is confused by two AGNs, PGC 13946 and ESO 201-IG 004 (**?**). These selections leave 103 AGNs that constitutes our "parent" sample (hereafter "Sample A").

The Swift/BAT AGNs are extensively followed-up by X-ray observatories covering below 10 keV, such as Swift/XRT, XMM-Newton, Suzaku, and Chandra. Key spectral parameters in our study are the absorption column density (N_{H}) and the fraction of scattered component (f_{scat}) for absorbed AGNs, which are often obtained by utilizing a partially covered absorber (or its equivalent) model. Because there can be other soft X-ray components that are spatially unresolved from the AGN emission, the f_{scat} value determined in this way is a upper limit to the true scattering fraction. Here we basically adopt the results of spectral analysis summarized in Table 1 of Ichikawa et al. (2012), which was largely based on Winter et al. (2009a) and was revised from (then) available Suzaku results for some targets. In our paper, we further revised their table by referring to later papers utilizing Suzaku data for more objects. Furthermore, for sources whose spectral parameters were not well constrained by using only the Swift/XRT data in Winter et al. (2009a), we update their spectral parameters according to **?**, who perform uniform broad-band spectral analysis in the 0.3–150 keV band by including Swift/BAT spectra for the whole AGN sample of the Swift/BAT 70 month catalog. We also utilize the 70-months averaged, de-absorbed 2–10 keV flux of the primary continuum listed in the **?** catalog, as well as the 9-months averaged 14–195 keV flux in the original Tueller et al. (2008) catalog.

We divide the sample into two types, X-ray unabsorbed AGNs (hereafter "X-ray type-1 AGNs") and absorbed AGNs ("X-ray type-2 AGNs"), which have absorptions of $\log N_{\mathrm{H}} < 22$ cm^{-2} and $\log N_{\mathrm{H}} \geq 22$, respectively. Among X-ray type-2 AGNs, we call those with $f_{\mathrm{scat}} < 0.5\%$ as low scattering-fraction AGNs (so-called "new type" AGNs), a putative population of AGNs deeply buried by geometrically thick tori. Due to our revision of the X-ray spectral parameters in the original Swift/BAT 9 month catalog, the sample of low scattering-fraction AGNs has been also updated[14] from that originally defined in Ichikawa et al. (2012).

Table 1 list the targets of Sample A with their basic X-ray properties: source number in Tueller et al. (2008) (** are attached to the low scattering-fraction AGNs), source name, redshift, N_{H}, f_{scat}, observed luminosity in the 14–195 keV band (9-month average), absorption-corrected 2–10 keV luminosity (70-month average), and reference for the X-ray spectral parameters. Though not listed in Table 1, we also compile the information on the inclination angle of the host galaxy, i_{host}, using the HyperLeda database, which are available for 98 AGNs [15]. In addition, the black hole mass (and hence an estimate of Eddington ratio) is available for 99 AGNs [16] from Winter et al. (2009a).

Figure 1 plots the host inclination against $\log N_{\mathrm{H}}$ for Sam-

[14] No. 51 and 120 are newly included in this sample while No. 4 and 86 are excluded.

[15] Except for No. 29, 31, 116, 124, 136, and 151 in Table 1

[16] Except for No. 23, 53, 87, 120, and 149 in Table 1

ple A. In all plots of our paper, the diagonal crosses correspond to X-ray type-1 (X-ray unabsorbed) AGNs and the filled circles to X-ray type-2 (X-ray absorbed) AGNs, among which the open circles denote those with low scattering fractions. As noticed, nine objects out of 10 with $i_{\rm host} > 85^\circ$ are X-ray type-2 AGNs, rejecting the null hypothesis that X-ray absorption is independent of the host inclination at $> 98\%$ confidence level. This is expected as galactic interstellar matter could produce an X-ray absorption of $\log N_{\rm H} > 22$ when viewed edge-on, and is in agreement with the deficiency of nearly edge-on Seyfert 1 galaxies reported by Keel (1980). Except for that, there is no correlation between $i_{\rm host}$ and $N_{\rm H}$. These results are consistent with the random distribution of the orientation angle of the torus (or the accretion disk) with respect to that of the galactic plane, confirming previous findings (Schmitt et al. 2001). We note that the $i_{\rm host}$ distribution of the AGNs with low scattering fractions in our sample are not concentrated at large values; more than half of this population are free from absorption by interstellar matter along the galactic disk, which therefore cannot account for their observed low scattering fractions. Indeed, a KS test for the $i_{\rm host}$ distribution between the low scattering-fraction AGNs and the rest of X-ray type-2 AGNs in Sample A yields a matching probability of 0.53. By considering the small sample size, this does not necessarily contradict the statistical result by Hönig et al. (2014); they obtain more edge-on dominant $i_{\rm host}$ distribution of the same population based on a slightly larger sample collected from the literature, although some of their sample are revised in our paper (see Section 2.1). We can conclude that there are at least two origins for their low scattering fractions, (1) intrinsic nature of the nucleus and (2) interstellar absorption in the host galaxy.

2.2. *Optical Observations at SAAO and Data Reduction*

We performed optical spectroscopic observations of Swift/BAT AGNs visible in the southern sky ($\delta < -10^\circ$) by using the SAAO 1.9-m telescope with the Cassegrain spectrograph during four observation runs: 2007 July, 2008 January, 2008 August, and 2009 February, each consists of roughly 14 nights. In this paper, we focus on sources in the Swift/BAT 9 month catalog, although our observation targets at the SAAO also include those in the Swift/BAT 22 month catalog, whose results will be reported in **?**. In total, the spectra of 38 AGNs have been analyzed in this work.

We used the 300 lines mm^{-1} grating, blazed at 6000 Å, covering about 4400-7600 Å, with a 2 arcsec slit-width placed on the center of each galaxy, producing a spectral resolution of $\approx$5 Å. The integration is split into a series of 150 second exposures, added up to a total integration time ranging from 750 to 3600 sec. Wavelength calibration of the spectra was obtained from CuAr arc lamp exposures taken during the same night. A flux calibration was obtained from long-slit (with 6 arcsec slit-width) observations of spectrophotometric standard stars. To derive the sensitivity curve, we fit the observed spectral energy distribution of the standard stars with a low-order polynomial.

The spectral line flux of [O III]λ5007, and those of narrow components of Hα and Hβ were measured using IRAF task *splot* from the co-added, dispersion corrected, and flux-calibrated spectra. If the lines were not significantly detected, we then estimated their upper limits (3σ) from the fluctuation of the noise level. The line fluxes are corrected for reddening from the Milky Way, by using the $E(B-V)$ map by Schlafly & Finkbeiner (2011) and the reddening curve by Cardelli, Clayton,& Mathis (1989) with R_V = 3.1. Finally, we approximately corrected these fluxes for the slit loss in the following way. For each dispersed spectrum, we projected the 4500–5500 Å region onto the spatial axis and measured its spread by fitting with a gaussian. We then calculated the fraction contained within the slit by assuming that the image is axisymmetric. By comparing the results of the same target taken on different days when available, we estimate that the flux uncertainties are typically of 0.1–0.2 dex, depending on the quality of the spectrum. This is similar to general errors in the [O III]λ5007 fluxes reported by Whittle (1992) when they are measured with small (2–4 arcsec) apertures. In some cases of broad line AGNs, we were unable to reliably measure the fluxes (nor the upper limits) of the narrow components of Hα and Hβ lines by separating them from the broad components.

2.3. *Catalog*

To complement the results from the SAAO observations, we gather [O III]λ5007, Hα, and Hβ fluxes in the literature for AGNs in the northern sky. We mainly adopt the results summarized by Winter et al. (2010a) except for those with too large uncertainties, and refer to other references (Mulchaey et al. 1994; Bassani et al. 1999; Xu et al. 1999; Landi et al. 2007; **?**) for the rest. We obtain constraints on the [O III]λ5007 flux for all 103 AGNs (48 X-ray type-1 and 55 X-ray type-2 AGNs) of the parent sample defined in Section 2.1 (Sample A), where one object (No. 49) does not show detectable [O III]λ5007 emission and hence has only an upper limit. Among them, 77 objects (31 X-ray type-1 and 46 X-ray type-2 AGNs) have reliable flux measurements (not upper limits) of both narrow Hα and Hβ emission lines, $F_{\rm H\alpha}$ and $F_{\rm H\beta}$, or their flux ratios, constituting "Sample B".

Table 1 lists the observed [O III]λ5007 luminosity ($L_{\rm [O\ III]}$) along with the fluxes of [O III]λ5007, narrow Hα, and narrow Hβ lines for Sample A with the reference of the optical spectroscopic data. For Sample B, we also calculate an extinction-corrected luminosity of [O III]λ5007 ($L^{\rm cor}_{\rm [O\ III]}$) from the Balmer decrement as

$$L^{\rm cor}_{\rm [O\ III]} = L_{\rm [O\ III]}\left(\frac{F_{\rm H\alpha}/F_{\rm H\beta}}{3.0}\right)^{2.94},$$

following Bassani et al. (1999). When the $F_{\rm H\alpha}/F_{\rm H\beta}$ ratio is smaller than 3.0, we do not apply any correction. As discussed in Hao et al. (2005), however, the intrinsic flux ratio between Hα and Hβ in the NLR of an AGN could be different from the value assumed here, being subject to the gas density and radiative transfer effects. Also, there is an uncertainty in the correction because the spatial distributions of the [O III]λ5007 and Balmer line emitting regions may not be the same due to the clumpiness of the NLR (see Section 4.1). Thus, we should regard these corrections only as approximation.

3. CORRELATIONS BETWEEN X-RAY AND OPTICAL LINE LUMINOSITIES

3.1. *Regression Analysis between X-ray and [O III]λ5007 Luminosities*

Figure 2 plots the correlation of the observed [O III]λ5007 luminosity ($\log L_{\rm [O\ III]}$) against (a) the luminosity in the 14–195 keV band ($\log L_{14-195}$) or (b) that in the 2–10 keV band ($\log L_{2-10}$), using Sample A. Figure 3 shows the same but for the [O III]λ5007 luminosity corrected for extinction ($\log L^{\rm cor}_{\rm [O\ III]}$), using Sample B. For each plot, we evaluate the

strength of the luminosity-luminosity and flux-flux correlations separately for X-ray type-1, X-ray type-2, and all (X-ray type-1 + type-2) AGNs; the resultant Spearman's rank coefficients and Student's t-null significance levels are summarized in Table 2. We also calculate the ordinary least square bisector regression lines of the luminosity-luminosity correlation with the form of $Y = a + bX$ where Y is either $\log L_{[\mathrm{O\ III}]}$ or $\log L^{\mathrm{cor}}_{[\mathrm{O\ III}]}$ and X is either $\log L_{14-195}$ or $\log L_{2-10}$. The parameters and their 1σ errors are listed in Table 2. The best-fit lines obtained from all AGNs are plotted in Figures 2 and 3. When Sample A is used, we ignore the two objects whose [O III]λ5007 luminosities are upper limits, and restrict the luminosity range above $\log L_{2-10} > 41$.

As shown in Table 2, we find significant correlations at confidence levels of $> 99\%$ between all combinations of the [O III]λ5007 and X-ray luminosities for any AGN types. The flux-flux correlations are weaker but significant at $> 90\%$ confidence levels; relatively weak correlation is obtained for the X-ray type-1 AGN sample, most probably due to the narrow X-ray flux range ($F_{\mathrm{X}} \simeq 2\times10^{-11} - 3\times10^{-10}$ erg cm^{-2} s^{-1} in the 14–195 keV band).

From the luminosity correlations for the entire AGN sample, we obtain $b \approx 1.2$ in the regression line, which is significantly ($> 1\sigma$) different from 1. This result is confirmed by the recent work based on a larger but less complete sample of Swift/BAT AGNs at $z > 0.01$ by Berney et al. (2015). We find that the slope for the X-ray type-1 AGNs is smaller than X-ray type-2 AGNs, although consistent within errors, given the large scatter of the correlations. The correlations with respect to L_{14-195} and those to L_{2-10} are found to be similar except for the normalizations. This is expected because absorption has a small effect on the observed hard X-ray luminosity (L_{14-195}) except for heavily Compton thick AGNs, and L_{2-10} is corrected for absorption through the X-ray spectral analysis.

We compare our results on the $L^{\mathrm{cor}}_{[\mathrm{O\ III}]}$ - L_{2-10} correlation obtained from X-ray type-2 AGNs with previous works. The slope we obtain, $b = 1.26 \pm 0.13$ (i.e., $L^{\mathrm{cor}}_{[\mathrm{O\ III}]} \propto L_{2-10}^{1.26\pm0.13}$), is somewhat larger than that of Lamastra et al. (2009), who derive $b = 0.98 \pm 0.06$ from a sample consisting of X-ray and optically selected Seyfert 2 galaxies. To check the effects of sample incompleteness of Sample B, we perform regression analysis with the *asurv* software (Isobe et al. 1986), by considering the lower limits of $L^{\mathrm{cor}}_{[\mathrm{O\ III}]}$ to be $L_{[\mathrm{O\ III}]}$ for the objects excluded in Sample B. We find that the slope b changes only by $\sim$0.01 compared with the case obtained from Sample B. Hence the sample incompleteness cannot explain the difference of our result from Lamastra et al. (2009). The reason behind the discrepancy is not clear, but could be due to the different sample selections and luminosity ranges. Lamastra et al. (2009) include a sample compiled by Panessa et al. (2006) from the Palomar optical spectroscopic survey, which covers a lower luminosity range ($L_{2-10} < 10^{42}$ erg s^{-1}) than our sample. In fact, Panessa et al. (2006) obtain a much smaller slope, $b = 0.75 \pm 0.09$, from their Seyfert 2 sample including Compton thick AGNs, whose intrinsic X-ray luminosities are simply estimated by multiplying by a constant factor. The flatter slope than ours would be explained if contamination of [O III]λ5007 from star formation in the host galaxy is more significant in lower luminosity AGNs (see Section 4.1). Another possibility is enhanced past activity in the low luminosity AGNs, which are left with a higher [O III]λ5007 luminosity with respect to the current low X-ray activity.

3.2. *Averaged [O III]λ5007 to X-ray Luminosity Ratio*

We calculate the error-weighted mean value of the [O III]λ5007 to X-ray luminosity ratio and its standard deviation for different AGN types. Here we consider a systematic error of 0.2 dex in $\log L_{[\mathrm{O\ III}]}$ and 0.5 dex in $\log L^{\mathrm{cor}}_{[\mathrm{O\ III}]}$ in addition to the errors listed in Table 1. The results are summarized in Table 3. Although we find that the best-fit regression line is not linear ($b > 1$), its effect can be checked by calculating an averaged $\log L_{\mathrm{X}}$ value in each sample, which is also listed in Table 3. In fact, we confirm that it little affects the following discussions.

As noticed from Table 3, we find that the mean ratio of observed [O III]λ5007 luminosity ($L_{[\mathrm{O\ III}]}$) to X-ray luminosity is significantly smaller in X-ray type-2 AGNs than in X-ray type-1 AGNs by $\approx$0.4 dex, using Sample A. This trend remains the same for the extinction-corrected [O III]λ5007 luminosity ($L^{\mathrm{cor}}_{[\mathrm{O\ III}]}$) obtained from Sample B, although the difference between X-ray type-1 and X-ray type-2 AGNs is reduced to 0.1–0.2 dex. The "reduction" is consistent with the fact that the mean extinction-correction factor is larger in X-ray type-2 AGNs ($< L^{\mathrm{cor}}_{[\mathrm{O\ III}]}/L_{[\mathrm{O\ III}]} > = 0.59 \pm 0.09$) than in X-ray type-1 AGNs ($< L^{\mathrm{cor}}_{[\mathrm{O\ III}]}/L_{[\mathrm{O\ III}]} > = 0.29 \pm 0.11$). This indicates a higher degree of obscuration toward the NLR in X-ray type-2 AGNs, consistent with previous results (e.g., Dahari & De Robertis 1988; Mulchaey et al. 1994; Meléndez et al. 2008). It may be explained if the torus, or its extended structure such as dusty outflow (Hönig et al. 2012), is large enough to block a part of the narrow-line region.

To investigate the nature of AGNs with low scattering fractions, we calculate the mean [O III]λ5007 to X-ray luminosity ratios for two subsamples of X-ray type-2 AGNs, (1) those with $f_{\mathrm{scat}} < 0.5\%$ and (2) those hosted by edge-on galaxies ($i_{\mathrm{host}} > 80°$). The results are also listed in Table 3. We find that the mean extinction-corrected [O III]λ5007 to X-ray luminosity ratio of the low scattering-fraction AGNs is much smaller than that of the total X-ray type-2 AGN sample, while that of the edge-on galaxies does not differ from it within uncertainties. A simple χ^2 test shows that the difference of the mean value of $L^{\mathrm{cor}}_{[\mathrm{O\ III}]}/L_{2-10}$ between the low scattering-fraction AGNs and the other X-ray type-2 AGNs is significant at $> 99.9\%$ confidence level. This is also noticeable from Figure 4(a), where we plot the $L^{\mathrm{cor}}_{[\mathrm{O\ III}]}/L_{2-10}$ ratio against $\log N_{\mathrm{H}}$ for Sample B.

These results suggest that a significant fraction of low scattering-fraction AGNs are indeed buried in a torus with very small opening angles as originally proposed by Ueda et al. (2007). This population of AGNs could contribute to reduce the averaged $L^{\mathrm{cor}}_{[\mathrm{O\ III}]}/L_{\mathrm{X}}$ ratio in the total X-ray type-2 AGN sample compared with that of X-ray type-1 AGNs, because they are predominantly identified as X-ray type-2 AGNs due to the large covering fraction by the torus. We can rule out the possibility that their low scattering fractions are merely the result of deficiency of scattering gas in the NLR. If this were the case, we should observe a similar fraction of low $L_{[\mathrm{O\ III}]}/L_{\mathrm{X}}$ objects among the X-ray type-1 AGN sample. Figure 4(b) plots the $L^{\mathrm{cor}}_{[\mathrm{O\ III}]}/L_{2-10}$ ratio against "X-ray Eddington ratio" (the 2–10 keV luminosity divided by the Eddington luminosity) using objects with available black hole masses in Winter et al. (2009a). No clear correlation is noticeable for the whole sample. The low scattering-fraction AGNs do not always have high Eddington ratios, while Noguchi et al. (2010) report a possible negative correlation between the scattering fraction and Eddington ratio. Theoretically, deeply

buried AGNs would be expected in the early growth phases of SMBHs with relatively small masses (hence with low luminosities). Thus, to further investigate the natures of this population, we need a larger sample of low luminosity AGNs.

3.3. *Correlations with Narrow Hα Line Luminosity*

In AGNs, intense narrow Hα and Hβ lines are also produced from the NLR. Hence, we also perform regression analysis between the narrow Hα and X-ray luminosities, and that between the narrow Hα and [O III]λ5007 luminosities, in the same way as done in Section 3.1. For each analysis, we utilize objects in Sample A that have available flux measurements of Hα or [O III]λ5007. The correlation plots are displayed in Figures 5 and 6, respectively, together with the best-fit linear regression forms, which are given in Table 2. We also calculate the mean and standard deviation of the $\log(L_{\rm H\alpha}/L_{2-10})$ ratio and the $\log(L_{\rm [O\ III]}/L_{\rm H\alpha})$ ratio, which are summarized in Table 3.

We find that, for all AGNs, (1) $L_{\rm H\alpha} \propto L_{2-10}^{1.02\pm0.08}$ with a similarly large scatter ($\approx$0.6 dex) to that seen in the $L_{\rm [O\ III]}$ vs. L_{2-10} correlation, and that (2) $L_{\rm [O\ III]} \propto L_{\rm H\alpha}^{1.19\pm0.05}$ with a much smaller scatter ($\approx$0.3 dex). The slope of the $L_{\rm H\alpha}$ vs. L_{2-10} correlation obtained from the X-ray type-2 AGNs, 1.04 ± 0.10, is larger than that obtained by Panessa et al. (2006) from their sample of 34 Seyfert 2s, 0.78 ± 0.09, which covers a lower luminosity range ($L_{2-10} < 10^{42}$ erg s^{-1}) than ours. Even though here we use only the luminosity of the "narrow" component of Hα, the regression slope and scatter between $L_{\rm H\alpha}$ and L_{2-10} are similar to those found between "total" $L_{\rm H\alpha}$ (i.e., that including the broad component) and L_{2-10} (e.g., Ho 2008).

4. DISCUSSION

4.1. *Origin of Correlation and Scatter between [O III]λ5007 and Hard X-ray Luminosities*

Using so far the largest ($N > 100$), statistically complete sample of hard X-ray ($E >$14 keV) selected AGNs in the local universe, we determine the statistical properties between [O III]λ5007 and hard X-ray luminosities with the best accuracy. The linear regression form of $L_{\rm [O\ III]} \propto L_{2-10}^{1.18\pm0.07}$ ($L_{\rm [O\ III]}^{\rm cor} \propto L_{2-10}^{1.16\pm0.09}$) is obtained from the whole sample (see Table 2). These results can be used as the reference for AGNs in the luminosity range of $\log L_{2-10} = 41-46$. We also find that the mean luminosity ratio between $L_{\rm [O\ III]}$ and L_{2-10} of X-ray type-2 AGNs is significantly smaller than that of X-ray type-1 AGNs. The difference is largely contributed by a population of low scattering-fraction AGNs. Another important result is the very large variance in the $\log(L_{\rm [O\ III]}/L_{2-10})$ ratio, corresponding to its standard deviation of $\sim$0.5 in X-ray type-1 AGNs and $\sim$0.7 in X-ray type-2 AGNs (see Table 3).

The non-linear correlation (i.e., $b \neq 1$) between $L_{\rm [O\ III]}$ and $L_{\rm X}$ may be explained by a combination of multiple effects. The first effect is the luminosity dependence of the AGN spectral energy distribution. The luminosity of the narrow lines is predominantly determined by the continuum flux of ultraviolet photons responsible for photo-ionization of the NLR gas, rather than the X-ray flux. Thus, if the spectral slope α (for the flux density $F_\nu \propto \nu^{-\alpha}$) between UV and hard X-rays above 2 keV is larger in more luminous AGNs as suggested by Scott & Stewart (2014), it works to make the [O III]λ5007 to X-ray luminosity correlation steeper. Secondly, according to the luminosity-dependent unification model (Ueda et al. 2003; Ricci et al. 2013), the opening angle of an torus increases with luminosity, thus making the angular spread of the "NLR cone" larger in more luminous AGNs. This also leads to increase b. The third effect is due to the luminosity dependence of the NLR size in the radial direction, which is proportional to $L^{0.33\pm0.04}$ (Schmitt et al. 2003). Thus, the actual size of the NLR might be saturated in very luminous AGNs if the outer radius exceeds the scale height of the host galaxy (Netzer et al. 2004). The fourth effect is the contamination of $L_{\rm [O\ III]}$ from star formation in low luminosity AGNs, as mentioned in Section 3.1. The last two effects make the regression slope flatter than unity.

To better understand the origin of the observed luminosity correlations and scatters between $L_{\rm [O\ III]}$ (or $L_{\rm [O\ III]}^{\rm cor}$) and $L_{\rm X}$, comparison with the $L_{\rm H\alpha}$ and $L_{\rm [O\ III]}$ correlation is useful. The Balmer lines are emitted by recombination as the result of photo-ionization, whereas the [O III]λ5007 line is emitted via collisional excitation in the heated gas. Thus, the intensity ratio between Hα and [O III]λ5007 depends on the physical parameters, such as the ionization parameter and density (Ferland & Netzer 1983). Also, the [O III]λ5007 line comes preferentially from gas with a density of $\sim 10^6$ cm^{-3} unlike the Balmer lines, which come from a wide range of densities. In fact, detailed images of the NLR with *Hubble* Space Telescope for a few low-z objects (e.g., Evans et al. 1991; Fischer et al. 2013) show that much of the [O III]λ5007 flux comes from clumpy structures. The effects of dust extinction inside the NLR, which may not be correctly measured with the Balmer decrement, makes it even more complex. Hence, depending on how the NLR gas and dust is distributed, non-linear correlation as well as a significant scatter in the flux ratio between the Balmer lines and [O III]λ5007 line would be also expected.

The results for all AGNs, $L_{\rm H\alpha} \propto L_{2-10}^{1.02\pm0.08}$ and $L_{\rm [O\ III]} \propto L_{\rm H\alpha}^{1.19\pm0.05}$, show that the observed non-linear correlation ($b \approx 1.2$) between $L_{\rm [O\ III]}$ and $L_{\rm X}$ cannot be simply explained by a single reason. In addition to the four possibilities listed above, it is found that the non-linear correlation between $L_{\rm [O\ III]}$ and $L_{\rm H\alpha}$, which is determined by plasma physics, also plays a role. The fact that the slope between $L_{\rm H\alpha}$ and L_{2-10} is close to unity ($b = 1.02 \pm 0.08$) indicates that the third effect (luminosity dependence of the NLR physical size) and/or the fourth effect (contamination by star formation) must work to cancel the first and second effects. The fact that flatter slopes are found from the X-ray type-1 AGNs, which are dominant in the largest luminosity range, suggest that the third effect is more important.

The large variation between $L_{\rm [O\ III]}$ and $L_{\rm X}$ may be explained because the optical emission lines from the NLR are a secondary indicator of the intrinsic AGN luminosity in that they do not directly come from near the SMBH and have strong dependence on the geometry and size of the NLR, its averaged density, clumpiness, and amount of dust. In fact, a significant scatter of $\sim$0.4 dex between the [O III]λ5007 luminosity and the continuum luminosity at 5100 Åis also reported in the SDSS quasar sample (Shen et al. 2011). The presence of the low scattering-fraction AGNs accounts for the larger scatter of the the $L_{\rm [O\ III]}/L_{\rm X}$ ratio in X-ray type-2 AGNs ($\sim$0.7 dex) than in X-ray type-1 AGNs ($\sim$0.5 dex), which could be understood in terms of variation in the geometry (cone angle) of the NLR. Since the correlation between $L_{\rm [O\ III]}$ and $L_{\rm H\alpha}$ is found to be tighter than that between $L_{\rm [O\ III]}$ and $L_{\rm X}$, the clumpiness of the NLR gas and dust extinction effects would not be the prime cause of the $L_{\rm [O\ III]}$- $L_{\rm X}$ scatter. Another effect could be time variability; even though we utilize

"70-month" averaged hard X-ray fluxes, the emission from the NLR reflects the past AGN power averaged over $> 10^2$ years.

4.2. *Comparison of [O III]λ5007, Hα, and X-ray luminosity functions*

The luminosity function (LF) is one of the most important statistical properties of AGNs. Utilizing an AGN sample selected from the *Sloan* Digital Sky Survey (SDSS), Hao et al. (2005) determined [O III]λ5007 and Hα LFs of AGNs at $z \leq 0.15$ (they adopt emission-line luminosities not corrected for extinction, and we follow the same procedure below.) Heckman et al. (2005) then compared the SDSS [O III]λ5007 LF with an X-ray LF in the 3–20 keV band derived from the *RXTE* Slew Survey by Sazonov & Revnivtsev (2004). They found that the X-ray LF significantly underpredicts the [O III]λ5007 LF when the mean luminosity ratio between $L_{\rm X}$ and $L_{\rm [O\ III]}$ obtained from the RXTE AGN sample is assumed without considering the scatter. On the basis of this result, they argue that X-ray surveys seem to miss a significant fraction of AGNs, particularly Compton-thick AGNs.

Recently, Ueda et al. (2014) determined the X-ray luminosity function of AGNs including Compton thick AGN over a redshift range of $z = 0-5$, using a highly complete sample of X-ray selected AGNs. The local AGN sample from the Swift/BAT survey is also utilized. Detection biases against (mildly) Compton thick AGNs are taken into account to correctly estimate their intrinsic number. Because heavily Compton thick AGNs with log $N_{\rm H}$ = 25–26 are difficult to detect even in the $E > 10$ keV hard X-ray band, they assume that the fraction of AGNs with log $N_{\rm H}$ = 25–26 is the same as those with log $N_{\rm H}$ = 24–25. The X-ray luminosity function and absorption distribution function are used as the basis of a standard population synthesis model of the X-ray background (Ueda et al. 2014). We note that the X-ray AGN LF by Sazonov & Revnivtsev (2004) may not be appropriate to adopt for direct comparison with LFs in other wavelengths because (1) the original X-ray LF by Sazonov & Revnivtsev (2004) was unfortunately affected by an error in the count rate to flux conversion (by a factor of 1.4; see Sazonov et al. 2008 and Ueda et al. 2011), (2) even after correcting for that error, it significantly underestimates other X-ray LFs of Compton thin AGNs (Ueda et al. 2011), and (3) Compton thick AGNs, which are difficult to detect in the 3–20 keV band, are not included.

Thus, it is very interesting to make comparison with the [O III]λ5007 and Hα LFs with the most up-to-date X-ray LF of local AGNs including Compton thick AGNs, in order to understand the completeness and cleanness of AGN selections in these different wavelengths. The red curve in Figures 7(a) and 7(b) represent the best-fit [O III]λ5007 and narrow Hα LFs in Hao et al. (2005) (two power-law model, the sum of Seyfert 1s and 2s), after correcting both luminosity and space density for the difference of the adopted Hubble constant, from H_0 = 100 km s^{-1} Mpc^{-1} (Hao et al. 2005) to H_0 = 70 km s^{-1} Mpc^{-1} (our paper). The black curve in each figure is a prediction for [O III]λ5007 (or Hα) LF calculated from the Ueda et al. (2014) X-ray LF at $z = 0$. Here we convert L_{2-10} into $L_{\rm [O\ III]}$ (or Hα) with the best-fit linear regression form (Table 2) separately for X-ray type-1 and X-ray type-2 AGNs, and also consider the scatter around it by assuming a gaussian distribution with the standard deviation listed in Table 3. As the Hao et al. (2005) result is obtained from AGNs at $z \leq 0.15$, we then multiply luminosity-dependent density evolution factors (Ueda et al. 2014) at the mean redshift. The black dashed curves denote the boundaries when both errors (1σ) in the mean and standard deviation of $\log(L_{\rm [O\ III]}/L_{2-10})$ (or $\log(L_{\rm H\alpha}/L_{2-10})$) are taken into account. For comparison, we also plot the case when the standard deviation is set to be zero (i.e., no scatter is considered) with the blue, dot-dashed curve.

As noticed from Figure 7(a), the [O III]λ5007 (red) and X-ray (black) LFs are roughly consistent with each other within a factor of ∼2 when we take into account the uncertainties in the $L_{\rm X}$ to $L_{\rm [O\ III]}$ conversion. Thus, the systematic (≈4) underestimate of the [O III]λ5007 LF by the X-ray LF over a wide range of luminosity reported by Heckman et al. (2005) is now resolved. Rather, at $\log L_{\rm [O\ III]} \gtrsim 40$, the X-ray LF outnumbers the [O III]λ5007 LF, while statistical uncertainties in the [O III]λ5007 LF are large (a factor of >2) at $\log L_{\rm [O\ III]} \gtrsim 41.6$ due to the limited sample size in the SDSS. Figure 7(b) shows even better agreement between the Hα and X-ray LFs over a wider luminosity range, although a similar discrepancy is noticed at $\log L_{\rm H\alpha} \gtrsim 41$. We note that it is important to consider the scatter between the two luminosities when making the comparison of LFs, as seen in the difference between the black solid curve (with scatter) and blue dot-dashed curve (without scatter).

These results confirm that hard X-ray (> 10 keV) observations are a very powerful tool to find AGNs with high completeness, not missing a dominant portion of the entire AGN population, once biases against Compton-thick AGNs are properly corrected (see e.g., Malizia et al. 2009). For the correction, however, it is essential to obtain the broad-band X-ray spectra covering up to, at least, a few tens of keV, with sufficiently good sensitivities. If the discrepancy between the [O III]λ5007 (or Hα) and X-ray LFs at the high luminosity range is true, this instead implies that the optical selection would miss some AGN populations. The selection based on emission-line diagrams could be incomplete for AGNs significantly contaminated by star formation; indeed, Winter et al. (2010a) show that a non negligible fraction of hard X-ray selected AGNs could be optically classified as H II galaxies, even though they are truly AGNs. Other candidates of "optically missing" AGNs are those deeply embedded in tori with almost spherical geometry, in which no or little NLR is formed. They may be similar to some of the low scattering-fraction AGNs in our sample whose [O III]λ5007 fluxes are very weak. If many of heavily Compton thick AGNs assumed in the Ueda et al. (2014) model correspond to this population, it would partially account for the mismatch between the optical and X-ray LFs.

5. CONCLUSIONS

From our observations at the SAAO and the literature, we have compiled a *complete* catalog of [O III]λ5007 line flux for 103 hard X-ray selected AGNs in the local universe located at $|b| > 15°$, together with narrow Hα and Hβ line fluxes (or their ratio) for a large fraction (∼80%) of the sample. The main conclusions are summarized below.

1. We detect significant correlations between [O III]λ5007 (without or with extinction correction) and X-ray luminosities independently from X-ray type-1 AGNs (log $N_{\rm H} < 22$) and X-ray type-2 AGNs (log $N_{\rm H} \geq 22$), even though there is a large scatter in their luminosity ratio. The best regression forms obtained from the whole sample are: $L_{\rm [O\ III]} \propto L_{\rm 2-10\ keV}^{1.18\pm0.07}$ and $L_{\rm [O\ III]}^{\rm cor} \propto L_{\rm 2-10\ keV}^{1.16\pm0.09}$.

2. Absorbed AGNs with low scattering fractions in the X-ray spectra show smaller $L_{[\mathrm{O\ III}]}/L_{\mathrm{X}}$ and $L^{\mathrm{cor}}_{[\mathrm{O\ III}]}/L_{\mathrm{X}}$ ratios than the other absorbed ones. This suggests that a significant part of low scattering-fraction AGNs are buried in tori with small opening angles.

3. Significant correlations are also found between the Hα and X-ray luminosities. The [O III]λ5007 and Hα luminosities are more tightly correlated than the [O III]λ5007 - X-ray luminosity correlation.

4. The X-ray luminosity function of local AGNs in a standard population synthesis model shows much better agreement with the [O III]λ5007 luminosity function derived from the SDSS than previously reported. It rather predicts a larger number of AGNs than the [O III]λ5007 selection at $\log L_{[\mathrm{O\ III}]} \gtrsim 40$. This confirms that hard X-ray (> 10 keV) observations are a very powerful tool to find AGNs with high completeness, once biases against Compton-thick AGNs are properly corrected on the basis of the broad-band X-ray spectra.

This paper uses observations made at the South African Astronomical Observatory (SAAO). Part of this work was financially supported by Grants-in-Aid for Scientific Research 26400228 (Y.U.) and for JSPS Fellows for Young Researchers (K.I.) from the Ministry of Education, Culture, Sports, Science and Technology (MEXT) of Japan, and by the National Science Council of Taiwan under the grants NSC 99-2112-M-003-001-MY2 and NSC 102-2112-M-003-016 (Y.H.). P.V. and A.Y.K. acknowledge the support from the National Research Foundation (NRF) of South Africa.

REFERENCES

Alonso-Herrero, A., Ward, M.J., & Kotilainen, J.K. 1997, MNRAS, 288, 977
Antonucci, R. 1993, ARA&A, 31, 473
Awaki, H., Anabuki, N., Fukazawa, Y., et al. 2008, PASJ, 60, 293
Ballantyne, D.R. 2005, MNRAS, 362, 1183
Bassani, L., Dadina, M., Maiolino, R., et al. 1999, ApJS, 121, 473
Berney, S., Koss, M., Trakhtenbrot, B., et al. 2015, MNRAS, 454, 3622
Bianchi, S., Piconcelli, E., Chiaberge, M., et al. 2009, ApJ, 695, 781
Cardelli, J.A., Clayton, G.C., & Mathis, J.S. 1989, ApJ, 345, 245
Comastri, A., Iwasawa, K., Gilli, R., et al. 2010, ApJ, 717, 787
Dahari, O. & De Robertis, M.M. 1988, ApJS, 67, 249
Eguchi, S., Ueda, Y., Terashima, Y., Mushotzky, R., & Tueller, J. 2009, ApJ, 696, 1657
Eguchi, S., Ueda, Y., Awaki, H., et al. 2011, ApJ, 729, 31
Evans, I.N., Ford, H.C., Kinney, A.L., et al. 1991, ApJ, 369, L27
Ferland, G.J. & Netzer, H. 1983, ApJ, 264, 105
Fischer, T.C., Crenshaw, D.M., Kraemer, S.B., & Schmitt, H.R. 2013, ApJS, 209, 1
González-Martín, O., Papadakis, I., Braito, V., et al. 2011, A&A, 527, A142
Hao, L., Strauss, M.A., Fan, X., et al. 2005, AJ, 129, 1795
Heckman, T.M., Ptak, A., Hornschemeier, A., & Kauffmann, G. 2005, ApJ, 634, 161
Ho, L.C. 2008, ARA&A, 46, 475
Hönig, S.F., Kishimoto, M., Antonucci, R., et al. 2012, ApJ, 755, 149
Hönig, S.F., Gandhi, P., Asmus, D., et al. 2014, MNRAS, 438, 647
Ichikawa, K., Ueda, Y., Terashima, Y., et al. 2012, ApJ, 754, 45
Ichikawa, K., Imanishi, M., Ueda, Y., et al. 2014, ApJ, 794, 139
Imanishi, M., Dudley, C.C., Maiolino, R., et al. 2007, ApJS, 171, 72
Isobe, T., Feigelson, E., & Nelson, P.I. 1986, ApJ, 306, 490
Keel, W.C. 1980, AJ, 85, 198
LaMassa, S.M., Heckman, T.M., Ptak, A., et al. 2009, ApJ, 705, 568
Lamastra, A,. Bianchi, S., Matt, G., et al. 2009, A&A, 504, 73
Landi, R., Masetti, N., Morelli, L., et al. 2007, ApJ, 669, 109
Malizia, A., Stephen, J.B., Bassani, L., et al. 2009, MNRAS, 399, 944
Meléndez, M., Kraemer, S.B., Armentrout, B.K., et al. 2008, ApJ, 682, 94
Mulchay, J.S., Koratkar, A., Ward, M.J., et al. 1994, ApJ, 436, 586
Netzer, H., Shemmer, O., Maiolino, R. et al. 2004, ApJ, 614, 558
Netzer, H., Mainieri, V., Rosati, P., & Trankhtenbrot, B 2006, A&A, 453, 525
Noguchi, K., Terashima, Y., Ishino, Y., et al. 2010, ApJ, 711, 144
Panessa, F., Bassani, L., Cappi, M., et al. 2006, A&A, 455, 173
Polletta, M., Bassani, L., Malaguti, G., Palumbo, G.G.C., & Caroli, E. 1996, ApJS, 106, 399
Ricci, C., Paltani, S., Awaki, H., et al. 2013, A&A, 553, A29
Risaliti, G., Braito, V., Laparola, V., et al. 2009, ApJ, 705, L1
Sazonov, S. & Revnivtsev, M. 2004, A&A, 423, 469
Sazonov, S., Krivonos, R., Revnivtsev, M., Churazov, E., & Sunyaev, R. 2008, A&A, 482, 517
Schlafly, E.F. & Finkbeiner, D.P. 2011, ApJ, 737, 103
Schmitt, H.R., Antonucci, R.R.J., Ulvestad, J.S., et al. 2001, ApJ, 555, 663
Schmitt, H.R., Donley, J.L., Antonucci, R.R.J., et al. 2003, ApJ, 597, 768
Scott, A.E. & Stewart, G.C. 2014, MNRAS, 438, 2253
Shen, Y., Richards, G.T., Strauss, M.A., et al. 2011, ApJS, 194, 45
Shirai, H., Fukazawa, Y., Sasada, M., et al. 2008, PASJ, 60, 263
Simpson, C. 2005, MNRAS, 360, 565
Toba, Y., Oyabu, S., Matsuhara, H., et al. 2014, ApJ, 788, 45
Tueller, J., Mushotzky, R.F., Barthelmy, S., et al. 2008, ApJ, 681, 113
Turner, T.J., Miller, L., Kraemer, S.B., Reeves, J.N., & Pounds, K.A. 2009, ApJ, 698, 99
Ueda, Y., Akiyama, M., Ohta, K., Miyaji, T. 2003, ApJ, 598, 886
Ueda, Y., Eguchi, S., Terashima, Y., et al. 2007, ApJ, 664, L79
Ueda, Y., Hiroi, K., Isobe, N., et al. 2011, PASJ, 63, 937
Ueda, Y., Akiyama, M., Hasinger, G., Miyaji, T., & Watson, M.G. 2014, ApJ, 786, 104
Whittle, M. 1992, ApJS, 79, 49
Winter, L.M., Mushotzky, R.F., Reynolds, C.S., & Tueller, J. 2009, ApJ, 690, 1322
Winter, L.M., Mushotzky, R.F., Terashima, Y., & Ueda, Y. 2009, ApJ, 701, 1644
Winter, L.M., Lewis, K.T., Koss, M., et al. 2010, ApJ, 710, 503
Winter, L.M., & Mushotzky, R.F. 2010, ApJ, 719, 737
Xu, C., Livio, M., & Baum, S. 1999, AJ, 118, 1169

TABLE 1
X-RAY AND OPTICAL EMISSION-LINE ([O III]λ5007, Hα, Hβ) PROPERTIES OF AGNS IN THE 9-MONTH *Swift*/BAT CATALOG

No.	Object	z	$\log L_{14-195}$ (erg s^{-1})	$\log L_{2-10}$ (erg s^{-1})	$\log N_{\rm H}$ (cm^{-2})	$f_{\rm scat}$	$\log L^{\rm cor}_{[\rm OIII]}$ (erg s^{-1})	$\log L_{[\rm OIII]}$ (erg s^{-1})	$\log F_{[\rm OIII]}$ (erg cm^{-2} s^{-1})	$\log F_{\rm H\alpha}$ (erg cm^{-2} s^{-1})	$\log F_{\rm H\beta}$ (erg cm^{-2} s^{-1})	References	
(1)	(2)	(3)	(4)	(5)	(6)	(7)	(8)	(9)	(10)	(11)	(12)	(X-ray) (13)	(Optical) (14)
1**	NGC 235A	0.0222	43.56	43.22	23.50	0.003	42.17± 0.43	41.23± 0.10	−12.82± 0.10	−13.17± 0.10	−13.96± 0.10	(xa)	(oa)
2**	Mrk 348	0.0150	43.68	43.30	23.20	0.004	41.95± 0.01	41.07± 0.01	−12.64± 0.01	−13.02± 0.01	−13.80± 0.01	(xb)	(ob)
3	Mrk 352	0.0149	43.27	42.74	20.75	···	···	40.39± 0.01	−13.31± 0.01	···	···	(xc)	(oc)
4	NGC 454	0.0121	42.88	42.17	23.30	0.030	>40.87	40.41± 0.20	−13.11± 0.20	−13.13± 0.20	<−13.77	(xa)	(oa)
5	Fairall 9	0.0470	44.39	44.15	20.36	···	···	42.15± 0.20	−12.56± 0.20	···	···	(xc)	(oa)
6	NGC 526A	0.0191	43.63	43.07	22.18	···	41.44± 0.43	41.32± 0.10	−12.59± 0.10	−13.08± 0.10	−13.59± 0.10	(xd)	(oa)
7	NGC 612	0.0298	43.81	43.45	24.05	0.006	40.09± 0.92	40.09± 0.13	−14.22± 0.13	−13.96± 0.11	−14.41± 0.29	(xe)	(od)
8**	ESO 297-G018	0.0252	43.85	43.67	23.81	0.003	41.43± 1.02	40.84± 0.04	−13.33± 0.04	−13.44± 0.21	−14.12± 0.27	(xf)	(od)
9	NGC 788	0.0136	43.39	43.22	23.67	0.007	40.91± 0.49	40.91± 0.18	−12.71± 0.18	−13.29± 0.01	−13.03± 0.16	(xd)	(oe)
10	Mrk 1018	0.0424	44.17	43.61	0.00	···	41.71± 0.65	41.71± 0.09	−12.91± 0.09	−13.46± 0.20	−13.91± 0.09	(xa)	(oe)
12	Mrk 590	0.0264	43.77	42.71	20.43	···	42.07± 0.12	41.74± 0.04	−12.46± 0.04	−13.00± 0.01	−13.59± 0.04	(xc)	(oe)
15	NGC 931	0.0167	43.66	43.41	21.56	···	41.91± 0.03	41.14± 0.01	−12.66± 0.01	−13.07± 0.01	−13.81± 0.01	(xd)	(od)
16	NGC 985	0.0430	44.21	43.78	21.59	···	42.75± 1.99	41.92± 0.01	−12.72± 0.01	−13.00± 0.01	−13.75± 0.68	(xc)	(od)
17	ESO 416-G002	0.0592	44.42	43.57	20.43	···	···	41.63± 0.20	−13.29± 0.20	···	···	(xc)	(oa)
18	ESO 198-024	0.0455	44.27	43.50	21.00	···	···	41.22± 0.20	−13.46± 0.20	···	···	(xc)	(oa)
20**	NGC 1142	0.0289	44.17	43.88	23.80	0.003	42.03± 0.03	41.07± 0.01	−13.21± 0.01	−13.30± 0.01	−14.10± 0.01	(xf)	(od)
23	PKS 0326–288	0.1080	44.84	44.42	23.82	0.009	43.58± 0.85	42.52± 0.20	−12.95± 0.20	−13.15± 0.20	−13.98± 0.20	(xa)	(oa)
24	NGC 1365	0.0055	42.67	42.03	24.65	0.260	40.98± 0.01	39.62± 0.01	−13.21± 0.01	(8.7)	···	(xg)	(of)
25	ESO 548-G081	0.0145	43.19	42.91	20.00	···	41.94± 0.08	40.99± 0.01	−12.69± 0.01	−12.65± 0.01	−13.45± 0.03	(xd)	(od)
28	2MASX J03565655–4041453	0.0747	44.51	43.70	22.66	0.032	42.56± 0.43	42.18± 0.10	−12.95± 0.10	−13.29± 0.10	−13.90± 0.10	(xa)	(oa)
29**	3C 105	0.0890	44.83	44.32	23.75	0.003	42.79± 0.10	41.59± 0.01	−13.70± 0.01	−14.10± 0.01	−14.99± 0.03	(xa)	(oe)
31	1H 0419–577	0.1040	44.91	44.60	24.31	···	43.55± 0.43	43.16± 0.10	−12.28± 0.10	−12.64± 0.10	−13.26± 0.10	(xh)	(oa)
32	3C 120	0.0330	44.45	43.98	21.20	···	···	41.86± 0.01	−12.54± 0.01	···	···	(xd)	(og)
34	MCG −01-13-025	0.0159	43.41	42.54	19.60	···	40.95± 0.03	40.73± 0.01	−13.02± 0.01	−13.21± 0.01	−13.76± 0.01	(xc)	(oe)
36	XSS J05054–2348	0.0350	44.24	43.49	23.47	0.009	41.65± 0.43	41.42± 0.10	−13.03± 0.10	−13.15± 0.10	−13.71± 0.10	(xf)	(oa)
38	Ark 120	0.0323	44.11	43.79	20.30	···	···	41.35± 0.01	−13.03± 0.01	···	···	(xd)	(oc)
39	ESO 362-G018	0.0126	43.26	42.88	23.43	0.087	···	40.88± 0.20	−12.67± 0.20	···	···	(xd)	(oa)
40	PICTOR A	0.0351	43.80	43.45	20.78	···	···	41.57± 0.20	−12.89± 0.20	···	···	(xd)	(oa)
45	NGC 2110	0.0078	43.54	43.17	22.45	0.048	41.64± 0.01	40.36± 0.01	−12.77± 0.01	−12.66± 0.01	−13.57± 0.01	(xd)	(ob)
47	EXO 055620–3820.2	0.0339	44.14	43.07	22.41	0.034	···	41.46± 0.10	−12.97± 0.10	···	···	(xd)	(oa)
49**	ESO 005-G004	0.0062	42.56	41.93	24.06	0.003	···	<38.63	<−14.30	−13.80± 0.01	<−15.39	(xf)	(oh)
50	Mrk 3	0.0135	43.61	43.35	24.04	0.009	43.33± 0.01	42.31± 0.01	−11.31± 0.01	−11.65± 0.01	−12.47± 0.01	(xi)	(oe)
51**	ESO 121-IG028	0.0403	44.03	43.63	23.31	0.004	>40.86	40.86± 0.24	−13.72± 0.24	−13.69± 0.10	<−13.76	(xa)	(oa)
53	2MASX J06403799–4321211	0.0610	44.40	43.51	23.00	<0.011	>41.74	41.74± 0.20	−13.21± 0.20	−13.19± 0.20	<−13.33	(xa)	(oa)
55	Mrk 6	0.0188	43.72	43.09	20.76	···	42.38± 1.56	42.38± 0.01	−11.52± 0.01	−11.97± 0.01	−12.41± 0.53	(xa)	(oe)
56	Mrk 79	0.0222	43.72	43.19	19.78	···	41.96± 0.12	41.96± 0.02	−12.09± 0.02	−12.66± 0.01	−13.11± 0.04	(xc)	(oe)
60	Mrk 18	0.0111	42.93	41.82	23.26	0.030	40.56± 0.28	40.56± 0.11	−12.88± 0.11	−12.72± 0.01	−12.98± 0.09	(xd)	(oe)
61	2MASX J09043699+5536025	0.0370	44.03	43.31	20.78	···	41.91± 0.09	41.63± 0.03	−12.87± 0.03	−12.95± 0.01	−13.52± 0.03	(xd)	(oe)
62	2MASX J09112999+4528060	0.0268	43.69	43.16	23.52	0.006	40.98± 0.11	39.68± 0.01	−14.54± 0.01	−14.49± 0.01	−15.41± 0.04	(xd)	(oe)
64	2MASX J09180027+0425066	0.1560	45.31	···	23.05	0.013	42.59± 0.01	42.22± 0.01	−13.60± 0.01	−14.08± 0.01	−14.68± 0.01	(xd)	(oe)
65	MCG −01-24-012	0.0196	43.60	43.24	22.81	0.005	41.10± 0.15	41.10± 0.08	−12.83± 0.08	−13.14± 0.01	−13.46± 0.05	(xa)	(oe)
66	MCG +04-22-042	0.0323	43.99	43.46	20.59	···	42.12± 0.62	42.12± 0.20	−12.26± 0.20	−12.57± 0.01	−12.72± 0.20	(xc)	(oe)
67	Mrk 110	0.0353	44.19	43.86	20.20	···	42.71± 0.59	42.29± 0.19	−12.17± 0.19	−12.47± 0.01	−13.09± 0.19	(xd)	(oe)
68	NGC 2992	0.0077	42.94	41.93	22.08	0.524	42.51± 0.43	40.76± 0.10	−12.36± 0.10	−12.48± 0.10	−13.55± 0.10	(xd)	(oa)
69	MCG −05-23-016	0.0085	43.55	43.21	22.20	···	>41.18	40.64± 0.10	−12.56± 0.10	−12.85± 0.10	<−13.50	(xd)	(oa)
70	NGC 3081	0.0080	43.09	42.96	23.99	0.006	41.66± 0.43	41.32± 0.10	−11.83± 0.10	−12.38± 0.10	−12.97± 0.10	(xe)	(oa)
71	NGC 3227	0.0039	42.63	42.05	22.24	0.148	41.26± 0.01	40.44± 0.01	−12.09± 0.01	−12.54± 0.01	−13.29± 0.01	(xd)	(ob)
72	NGC 3281	0.0107	43.27	42.69	23.94	0.019	41.42± 0.85	41.05± 0.20	−12.36± 0.20	−12.71± 0.20	−13.31± 0.20	(xd)	(oa)
75**	Mrk 417	0.0328	43.95	43.73	23.93	0.002	41.19± 0.05	40.92± 0.01	−13.48± 0.01	−13.76± 0.01	−14.33± 0.02	(xd)	(oe)
77	NGC 3516	0.0088	43.26	42.72	21.55	···	41.54± 0.01	40.92± 0.01	−12.32± 0.01	(4.9)	···	(xd)	(oc)
78	RX J1127.2+1909	0.1055	44.79	43.84	0.00	···	43.02± 0.14	43.02± 0.11	−12.43± 0.11	−13.03± 0.01	−13.42± 0.03	(xa)	(oe)
79	NGC 3783	0.0097	43.53	43.30	21.76	0.278	···	41.47± 0.10	−11.85± 0.10	···	···	(xd)	(oa)
80	SBS 1136+594	0.0601	44.33	43.82	0.00	···	42.70± 0.06	42.55± 0.01	−12.39± 0.01	−12.92± 0.01	−13.45± 0.02	(xa)	(oe)
81	UGC 06728	0.0065	42.54	41.94	20.00	···	40.22± 0.01	40.22± 0.01	−12.75± 0.01	−12.34± 0.01	−12.80± 0.01	(xd)	(oe)
82	2MASX J11454045–1827149	0.0330	43.98	43.64	0.00	···	42.19± 0.43	42.19± 0.10	−12.21± 0.10	−12.91± 0.10	−13.36± 0.10	(xa)	(oa)
83	CGCG 041–020	0.0360	43.88	43.39	23.03	0.009	41.17± 0.07	40.38± 0.01	−14.10± 0.01	−13.96± 0.01	−14.70± 0.02	(xd)	(oe)
85	NGC 4051	0.0023	41.74	41.33	20.46	···	40.41± 0.56	40.20± 0.18	−11.87± 0.18	−11.97± 0.01	−12.52± 0.18	(xc)	(oe)
86	Ark 347	0.0224	43.42	42.90	23.36	0.016	41.53± 0.22	41.53± 0.19	−12.52± 0.19	−13.08± 0.01	−13.31± 0.04	(xa)	(oe)
87	NGC 4102	0.0028	41.62	41.41	24.30	···	40.72± 0.02	38.78± 0.01	−13.46± 0.01	−12.48± 0.01	−13.62± 0.01	(xj)	(od)
88	NGC 4138	0.0030	41.62	41.23	22.90	0.012	38.95± 0.01	38.95± 0.01	−13.35± 0.01	−13.33± 0.01	−13.72± 0.01	(xd)	(od)
89	NGC 4151	0.0033	42.96	42.58	22.73	0.041	41.87± 0.24	41.87± 0.01	−10.51± 0.01	−11.12± 0.01	−11.40± 0.08	(xd)	(oe)
90	Mrk 766	0.0129	42.94	42.67	21.72	···	42.03± 0.13	41.79± 0.01	−11.78± 0.01	−12.10± 0.04	−12.66± 0.02	(xc)	(oe)
91	NGC 4388	0.0084	43.60	43.17	23.53	0.011	41.29± 0.13	41.29± 0.11	−11.90± 0.11	−12.33± 0.01	−12.80± 0.03	(xk)	(oe)
92	NGC 4395	0.0011	40.81	40.64	22.52	0.322	39.02± 0.01	38.93± 0.01	−12.49± 0.01	−12.81± 0.01	−13.32± 0.01	(xd)	(oe)
94	NGC 4507	0.0118	43.78	43.54	23.54	0.029	42.12± 0.43	41.76± 0.10	−11.73± 0.10	−12.10± 0.10	−12.70± 0.10	(xd)	(oa)
95**	ESO 506-G027	0.0250	44.28	43.95	23.92	0.002	>41.14	40.96± 0.20	−13.19± 0.20	−13.67± 0.20	<−14.20	(xl)	(oa)
96	XSS J12389–1614	0.0366	44.26	43.35	22.63	0.043	41.88± 0.85	41.87± 0.20	−12.63± 0.20	−12.81± 0.20	−13.29± 0.20	(xa)	(oa)
97	NGC 4593	0.0090	43.21	42.81	20.49	···	41.04± 0.01	40.50± 0.01	−12.76± 0.01	(4.6)	···	(xd)	(oc)
100	SBS 1301+540	0.0299	43.72	43.09	20.60	···	41.25± 0.21	41.25± 0.01	−13.06± 0.01	−13.54± 0.07	−13.87± 0.01	(xc)	(oe)
102**	NGC 4992	0.0251	43.83	43.17	23.75	<0.003	39.85± 0.16	39.85± 0.01	−14.30± 0.01	−14.50± 0.02	−14.82± 0.05	(xm)	(od)
103	MCG −03-34-064	0.0165	43.46	43.95	23.61	0.039	42.55± 0.43	42.21± 0.10	−11.57± 0.10	−12.13± 0.10	−12.73± 0.10	(xd)	(oa)
105	MCG −06-30-015	0.0077	43.00	42.74	21.28	···	···	40.23± 0.20	−12.89± 0.20	···	···	(xd)	(oa)
106	NGC 5252	0.0230	43.90	43.39	22.64	0.038	40.79± 0.01	40.37± 0.01	−13.71± 0.01	−13.32± 0.01	−13.94± 0.01	(xd)	(oe)
108	IC 4329A	0.0160	44.24	43.84	21.79	···	41.62± 0.19	41.02± 0.04	−12.74± 0.04	−13.09± 0.04	−13.77± 0.04	(xd)	(od)
109	Mrk 279	0.0304	43.97	43.42	20.11	···	41.76± 0.21	41.68± 0.01	−12.65± 0.01	−13.01± 0.01	−13.51± 0.07	(xd)	(od)
110	NGC 5506	0.0062	43.30	42.91	22.44	0.011	41.89± 0.11	41.03± 0.08	−11.90± 0.08	−11.99± 0.01	−12.76± 0.03	(xd)	(oe)
112	NGC 5548	0.0172	43.59	43.14	20.85	···	42.13± 0.06	42.13± 0.02	−11.69± 0.02	−12.37± 0.01	−12.74± 0.02	(xd)	(oe)
113	ESO 511-G030	0.0224	43.73	43.41	20.99	···	···	40.62± 0.20	−13.44± 0.20	···	···	(xd)	(oa)
115	NGC 5728	0.0093	43.23	43.03	24.14	0.007	41.96± 0.43	41.52± 0.10	−11.76± 0.10	−12.23± 0.10	−12.85± 0.10	(xm)	(oa)
116	Mrk 841	0.0364	44.20	43.87	21.34	···	41.64± 0.04	41.64± 0.01	−12.85± 0.01	−13.37± 0.01	−13.79± 0.01	(xc)	(od)
117	Mrk 290	0.0296	43.79	42.93	21.18	···	41.71± 0.50	41.59± 0.01	−12.71± 0.01	−13.20± 0.01	−13.72± 0.17	(xd)	(od)
118	Mrk 1498	0.0547	44.50	44.05	23.10	0.016	42.43± 0.31	42.43± 0.20	−12.42± 0.20	−13.18± 0.01	−13.05± 0.08	(xf)	(oe)
120**	NGC 6240	0.0245	43.81	44.16	24.25	<0.005	42.12± 0.12	40.71± 0.02	−13.43± 0.02	−12.73± 0.01	−13.69± 0.04	(xa)	(oe)
124	1RXS J174538.1+290823	0.1113	45.09	44.37	0.00	···	···	42.75± 0.03	−12.75± 0.03	···	···	(xa)	(oe)
125	3C 382	0.0579	44.81	44.67	20.11	···	42.31± 0.08	41.70± 0.01	−13.20± 0.01	−13.36± 0.01	−14.04± 0.03	(xc)	(od)
126**	ESO 103-035	0.0133	43.58	43.38	23.33	0.001	42.20± 0.85	40.87± 0.20	−12.73± 0.20	−12.80± 0.20	−13.73± 0.20	(xd)	(oa)
127	3C 390.3	0.0561	44.88	44.52	21.08	···	42.96± 0.38	42.72± 0.01	−12.15± 0.01	−12.51± 0.13	−13.06± 0.02	(xd)	(od)
129	NGC 6814	0.0052	42.57	42.22	20.76	···	···	40.17± 0.10	−12.61± 0.10	···	···	(xc)	(oa)
133	NGC 6860	0.0149	43.39	42.89	21.00	···	···	40.93± 0.10	−12.76± 0.10	···	···	(xn)	(oa)
136	4C +74.26	0.1040	45.14	44.87	21.25	···	43.37± 0.61	43.13± 0.17	−12.31± 0.17	−12.83± 0.01	−13.39± 0.20	(xo)	(oe)
137	Mrk 509	0.0344	44.43	44.08	20.18	···	···	42.17± 0.20	−12.26± 0.20	···	···	(xd)	(oa)
138	IC 5063	0.0114	43.31	43.08	23.40	0.009	42.26± 0.43	41.58± 0.10	−11.88± 0.10	−12.20± 0.10	−12.91± 0.10	(xh)	(oa)
139	2MASX J21140128+8204483	0.0840	44.80	44.35	0.00	···	>43.60	42.89± 0.01	−12.35± 0.01	−12.54± 0.04	<−13.25	(xa)	(od)
144	UGC 11871	0.0266	43.80	43.26	22.32	0.016	42.56± 0.01	41.45± 0.01	−12.76± 0.01	−12.25± 0.01	−13.10± 0.01	(xa)	(oe)
145**	NGC 7172	0.0087	43.32	42.90	22.91	0.001	39.94± 0.85	39.94± 0.20	−13.28± 0.20	−13.55± 0.20	−13.75± 0.20	(xd)	(oa)
146	NGC 7213	0.0058	42.59	41.85	20.40	···	40.23± 0.85	40.23± 0.20	−12.64± 0.20	−12.39± 0.20	−12.83± 0.20	(xd)	(oa)
147	NGC 7314	0.0048	42.45	41.96	21.60	···	40.25± 0.43	39.78± 0.10	−12.93± 0.10	−13.21± 0.10	−13.85± 0.10	(xd)	(oa)
148**	NGC 7319	0.0225	43.68	43.40	23.82	0.004	40.72± 0.20	40.72± 0.03	−13.34± 0.03	−13.68± 0.01	−13.86± 0.07	(xa)	(oe)
149	3C 452	0.0811	44.73	43.83	23.36	0.064	42.09± 0.09	40.98± 0.01	−14.23± 0.01	−14.22± 0.01	−15.07± 0.03	(xd)	(oe)
151	MR 2251–178	0.0640	45.03	44.60	21.45	···	42.87± 0.43	42.33± 0.10	−12.66± 0.10	−12.89± 0.10	−13.55± 0.10	(xd)	(oa)
152	NGC 7469	0.0163	43.70	42.97	20.61	···	43.14± 0.01	41.70± 0.01	−12.08± 0.01	−11.89± 0.01	−12.85± 0.01	(xc)	(ob)
153	Mrk 926	0.0469	44.45	44.19	20.54	···	42.66± 0.03	42.66± 0.01	−12.05± 0.01	−12.68± 0.01	−13.05± 0.01	(xd)	(oe)
154	NGC 7582	0.0052	42.61	42.65	23.80	0.033	41.26± 0.43	40.38± 0.10	−12.39± 0.10	−12.10± 0.10	−12.88± 0.10	(xp)	(oa)

TABLE 1 — CONTINUED

No.	Object	z	$\log L_{14-195}$ (erg s^{-1})	$\log L_{2-10}$ (erg s^{-1})	$\log N_{\rm H}$ (cm^{-2})	$f_{\rm scat}$	$\log L^{\rm cor}_{\rm [OIII]}$ (erg s^{-1})	$\log L_{\rm [OIII]}$ (erg s^{-1})	$\log F_{\rm [OIII]}$ (erg cm^{-2}s^{-1})	$\log F_{\rm H\alpha}$ (erg cm^{-2} s^{-1})	$\log F_{\rm H\beta}$ (erg cm^{-2} s^{-1})	References	
												(X-ray)	(Optical)
(1)	(2)	(3)	(4)	(5)	(6)	(7)	(8)	(9)	(10)	(11)	(12)	(13)	(14)

NOTE. — This table summarizes X-ray and optical emission line ([O III]λ5007, Hα, Hβ) properties of 95 *Swift*/BAT 9-month AGNs in Tueller et al. (2008) excluding Cen A, blazars, and those at low Galactic latitudes ($|b| < 15^\circ$). Columns:: (1) source no. in Tueller et al. (2008); (2) object name; (3) redshift; (4) 9-month averaged 14–195 keV luminosity calculated from the observed flux; (5) absorption-corrected 2–10 keV luminosity of the transmitted component averaged for 70 months; (6) X-ray absorption hydrogen column density (0.00 means $N_{\rm H} = 0$); (7) soft X-ray scattering fraction; (8) [O III]λ5007 luminosity corrected for extinction based on the Balmer decrement; (9) observed [O III]λ5007 luminosity (with no extinction correction); (10) [O III]λ5007 flux; (11) narrow Hα flux (number in parenthesis refers to Hα/ Hβ flux ratio); (12) narrow Hβ flux; (13) reference for the X-ray spectra (Columns 6 and 7): (xa) **?**, (xb) Noguchi et al. (2010), (xc) Tueller et al. (2008), (xd) Winter et al. (2009a), (xe) Eguchi et al. (2011), (xf) Eguchi et al. (2009), (xg) Risaliti et al. (2009) (xh) Turner et al. (2009), (xi) Awaki et al. (2008), (xj) González-Martín et al. (2011), (xk) Shirai et al. (2008), (xl) Winter et al. (2009b), (xm) Comastri et al. (2010), (xn) Winter & Mushotzky (2010b), (xo) Ballantyne (2005), (xp) bia Bianchi et al. (2009). (14) reference for the optical line fluxes (Columns 8–12): (oa) this work, (ob) Dahari & De Robertis (1988), (oc) Mulchaey et al. (1994), (od) **?**, (oe) Winter et al. (2010a), (of) Bassani et al. (1999), (og) Xu et al. (1999), (oh) Landi et al. (2007). Columns (1)–(4) are taken from Tueller et al. (2008) except for the revised redshift of no. 53 (2MASX J06403799–4321211). Column (5) is taken from C. Ricci et al. (2015, in preparation). All luminosities are calculated from the redshift given in column (3) with (H_0, $\Omega_{\rm m}$, Ω_λ) = (70 km s^{-1} Mpc^{-1}, 0.3, 0.7).

TABLE 2
CORRELATION PROPERTIES BETWEEN DIFFERENT LUMINOSITIES

Y (1)	X (2)	Sample (3)	N (4)	ρ_L (5)	ρ_f (6)	P_L (7)	P_f (8)	a (9)	b (10)
$\log L_{[\mathrm{O\ III}]}$	$\log L_{14-195}$	All	101	0.672	0.419	1.4×10^{-14}	1.3×10^{-5}	-11.0 ± 2.9	1.20 ± 0.07
		Type 1	48	0.781	0.240	5.9×10^{-11}	1.0×10^{-1}	-8.0 ± 3.8	1.13 ± 0.09
		Type 2	53	0.461	0.548	5.1×10^{-4}	2.2×10^{-5}	-10.3 ± 3.7	1.18 ± 0.09
$\log L_{[\mathrm{O\ III}]}$	$\log L_{2-10}$	All	100	0.630	0.375	2.1×10^{-12}	1.2×10^{-4}	-10.0 ± 2.9	1.18 ± 0.07
		Type 1	48	0.761	0.239	3.4×10^{-10}	1.0×10^{-1}	-5.5 ± 3.6	1.08 ± 0.09
		Type 2	52	0.447	0.488	9.1×10^{-4}	2.4×10^{-4}	-10.2 ± 4.0	1.19 ± 0.10
$\log L^{\mathrm{cor}}_{[\mathrm{O\ III}]}$	$\log L_{14-195}$	All	76	0.594	0.475	1.5×10^{-8}	1.5×10^{-5}	-9.8 ± 4.0	1.18 ± 0.09
		Type 1	31	0.705	0.341	9.5×10^{-6}	6.0×10^{-2}	-5.4 ± 4.2	1.08 ± 0.10
		Type 2	45	0.421	0.571	4.0×10^{-3}	4.2×10^{-5}	-12.0 ± 5.5	1.23 ± 0.13
$\log L^{\mathrm{cor}}_{[\mathrm{O\ III}]}$	$\log L_{2-10}$	All	75	0.619	0.516	3.2×10^{-9}	2.2×10^{-6}	-8.5 ± 3.7	1.16 ± 0.09
		Type 1	31	0.716	0.463	5.9×10^{-6}	8.8×10^{-3}	-1.6 ± 3.5	1.01 ± 0.09
		Type 2	44	0.503	0.552	5.0×10^{-4}	1.0×10^{-4}	-12.8 ± 5.3	1.26 ± 0.13
$\log L_{\mathrm{H}\alpha}$	$\log L_{2-10}$	All	82	0.608	0.352	1.4×10^{-9}	1.2×10^{-3}	-3.0 ± 3.1	1.02 ± 0.08
		Type 1	32	0.739	0.128	1.3×10^{-6}	4.8×10^{-1}	3.9 ± 3.9	0.87 ± 0.09
		Type 2	50	0.542	0.514	4.9×10^{-5}	1.3×10^{-4}	-4.0 ± 4.2	1.04 ± 0.10
$\log L_{[\mathrm{O\ III}]}$	$\log L_{\mathrm{H}\alpha}$	All	82	0.934	0.851	2.1×10^{-37}	4.6×10^{-24}	-7.6 ± 2.1	1.19 ± 0.05
		Type 1	32	0.937	0.799	3.1×10^{-15}	4.1×10^{-8}	-6.2 ± 2.7	1.16 ± 0.07
		Type 2	50	0.886	0.877	1.2×10^{-17}	6.4×10^{-17}	-7.6 ± 3.1	1.03 ± 0.11

NOTE. — Columns: (1) Y variable; (2) X variable; (3) AGN type; (4) number of sample; (5) Spearman's rank coefficient for luminosity–luminosity correlation (ρ_{L}); (6) Spearman's rank coefficient for flux–flux correlation (ρ_{f}); (7) Student's t-null significance level for luminosity–luminosity correlation (P_{L}); (8) Student's t-null significance level for flux–flux correlation (P_{f}); (9) regression intercept (a) and its 1σ uncertainty; (10) slope (b) and its 1σ uncertainty. Equation is represented as $Y = a+bX$.

TABLE 3
SUMMARY OF LUMINOSITY RATIOS

Luminosity Ratio	Sample (1)	N (2)	$< r >$ (3)	σ (4)	$< L_{\mathrm{X}} >$ (5)
$\log(L_{[\mathrm{O\ III}]}/L_{14-195})$	All	102	-2.45 ± 0.06	0.60 ± 0.05	43.71
	Type 1	48	-2.27 ± 0.07	0.47 ± 0.05	43.85
	Type 2	54	-2.62 ± 0.10	0.66 ± 0.07	43.60
	Type 2 ($f_{\mathrm{scat}}<0.5\%$)	12	-3.13 ± 0.10	0.33 ± 0.08	43.92
	Type 2 ($i_{\mathrm{host}}>80°$)	10	-2.43 ± 0.13	0.41 ± 0.10	43.24
$\log(L_{[\mathrm{O\ III}]}/L_{2-10})$	All	101	-1.99 ± 0.07	0.63 ± 0.05	43.24
	Type 1	48	-1.78 ± 0.08	0.51 ± 0.06	43.36
	Type 2	53	-2.19 ± 0.10	0.67 ± 0.07	43.14
	Type 2 ($f_{\mathrm{scat}}<0.5\%$)	12	-2.85 ± 0.09	0.31 ± 0.07	43.62
	Type 2 ($i_{\mathrm{host}}>80°$)	10	-2.01 ± 0.17	0.53 ± 0.13	42.81
$\log(L^{\mathrm{cor}}_{[\mathrm{O\ III}]}/L_{14-195})$	All	77	-1.94 ± 0.08	0.69 ± 0.06	43.65
	Type 1	31	-1.89 ± 0.09	0.48 ± 0.07	43.79
	Type 2	46	-1.98 ± 0.12	0.80 ± 0.09	43.56
	Type 2 ($f_{\mathrm{scat}}<0.5\%$)	9	-2.44 ± 0.28	0.82 ± 0.21	43.87
	Type 2 ($i_{\mathrm{host}}>80°$)	7	-1.63 ± 0.23	0.59 ± 0.17	43.06
$\log(L^{\mathrm{cor}}_{[\mathrm{O\ III}]}/L_{2-10})$	All	76	-1.48 ± 0.08	0.69 ± 0.06	43.18
	Type 1	31	-1.38 ± 0.10	0.51 ± 0.07	43.28
	Type 2	45	-1.55 ± 0.12	0.78 ± 0.09	43.11
	Type 2 ($f_{\mathrm{scat}}<0.5\%$)	9	-2.16 ± 0.24	0.71 ± 0.18	43.58
	Type 2 ($i_{\mathrm{host}}>80°$)	7	-1.20 ± 0.29	0.76 ± 0.22	42.62
$\log(L_{\mathrm{H}\alpha}/L_{2-10})$	All	83	-2.18 ± 0.07	0.61 ± 0.05	43.22
	Type 1	32	-1.95 ± 0.10	0.54 ± 0.07	43.36
	Type 2	51	-2.35 ± 0.09	0.60 ± 0.07	43.14
	Type 2 ($f_{\mathrm{scat}}<0.5\%$)	13	-2.97 ± 0.08	0.28 ± 0.06	43.49
	Type 2 ($i_{\mathrm{host}}>80°$)	11	-2.28 ± 0.18	0.57 ± 0.13	42.73
$\log(L_{[\mathrm{O\ III}]}/L_{\mathrm{H}\alpha})$	All	83	0.23 ± 0.04	0.32 ± 0.03	41.06
	Type 1	32	0.32 ± 0.05	0.27 ± 0.04	41.40
	Type 2	51	0.16 ± 0.05	0.34 ± 0.04	40.85
	Type 2 ($f_{\mathrm{scat}}<0.5\%$)	12	0.15 ± 0.09	0.30 ± 0.07	40.63
	Type 2 ($i_{\mathrm{host}}>80°$)	10	0.26 ± 0.06	0.17 ± 0.05	40.52

NOTE. — Columns: (1) luminosity ratio; (2) AGN type; (3) number of objects; (4) average; (5) standard deviation; (6) mean luminosity value of the denominator in the sample.

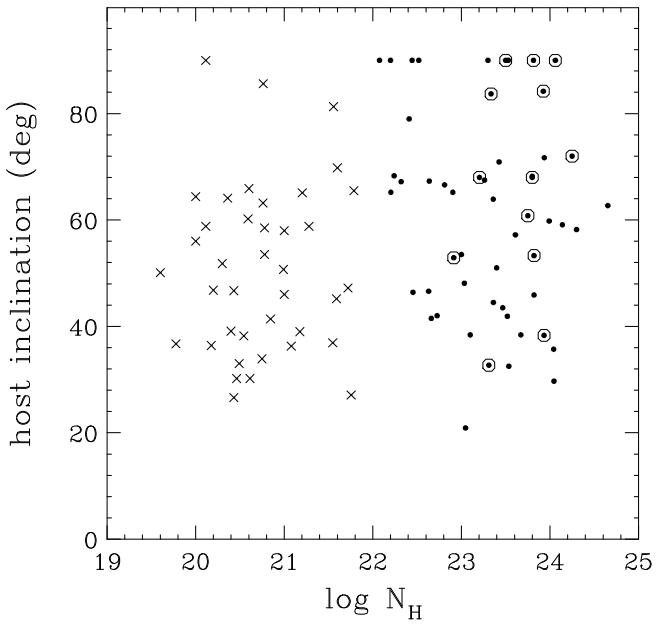

FIG. 1.— Plot of host-galaxy inclination ($i_{\rm host}$) versus X-ray absorption column density ($N_{\rm H}$) for Sample A (see Section 2.3). The diagonal crosses, filled circles, filled+open circles correspond to the X-ray type-1 (unabsorbed) AGNs, X-ray type-2 (absorbed) AGNs, and X-ray type-2 AGNs with low scattering fractions.

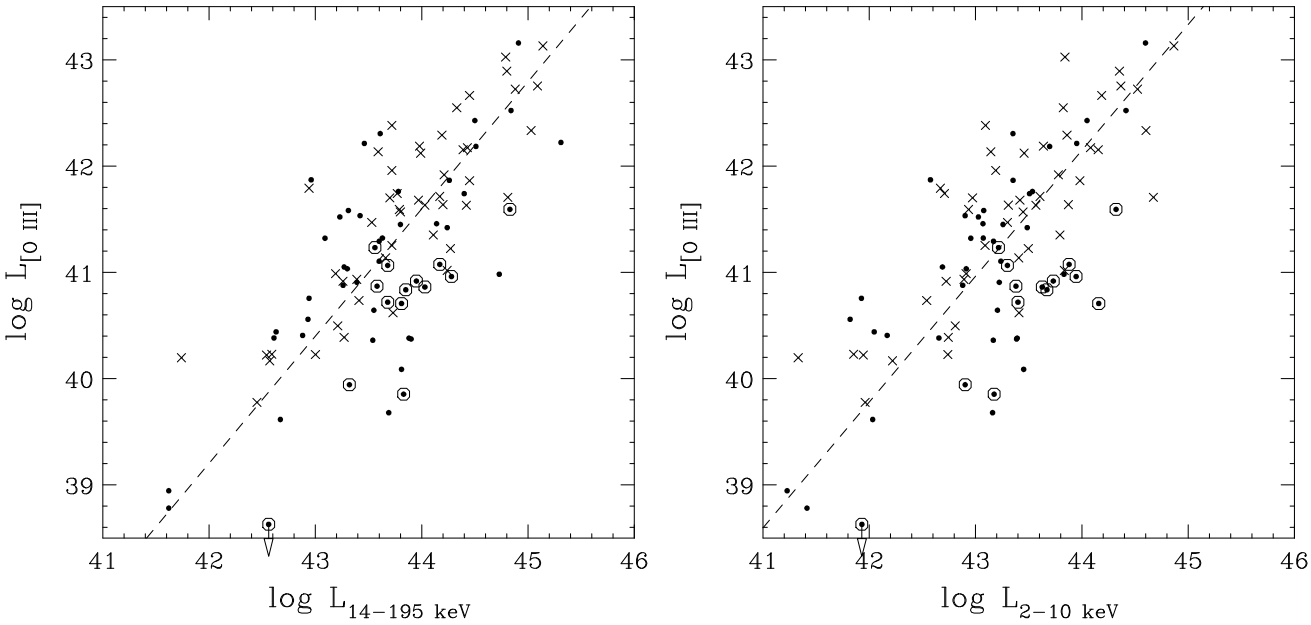

FIG. 2.— *Left*: (a) Correlation between the observed X-ray luminosity in the 14–195 keV band and observed [O III]λ5007 luminosity for Sample A. *Right*: (b) Correlation between the intrinsic X-ray luminosity in the 2–10 keV band and observed [O III]λ5007 luminosity for Sample A. The lines are the best-fit regression lines obtained from all (X-ray type-1 and X-ray type-2) AGNs. The symbols are the same as in Figure 1.

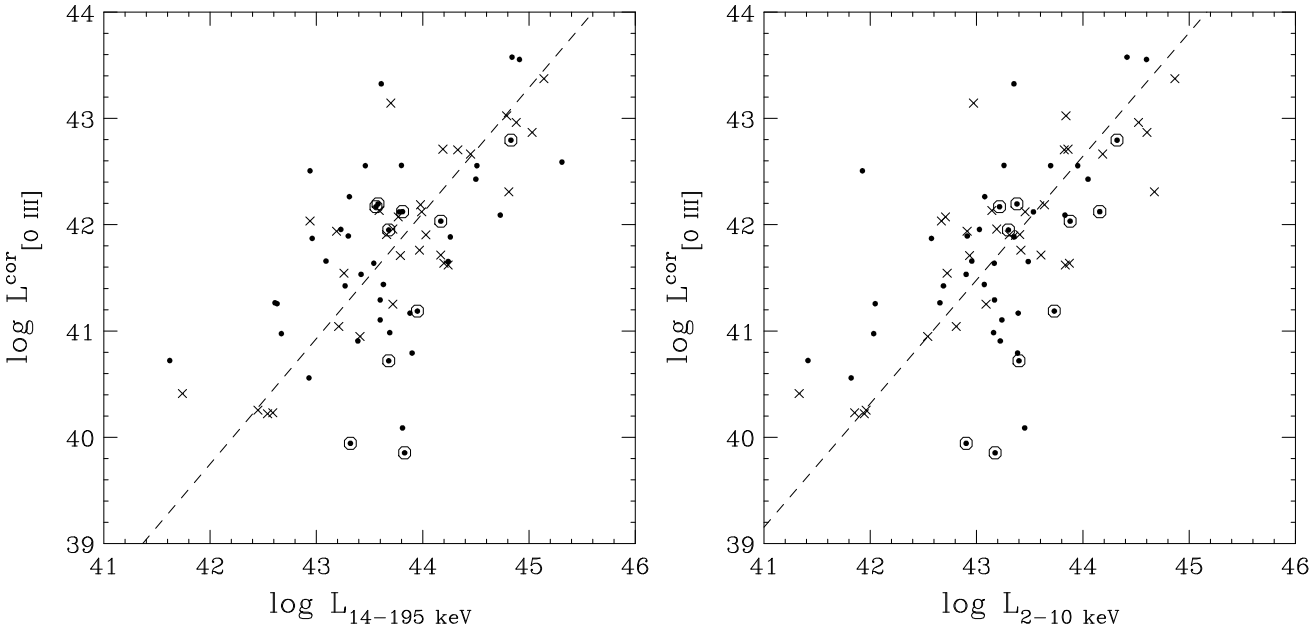

FIG. 3.— *Left*: (a) Correlation between the observed X-ray luminosity in the 14–195 keV band and extinction-corrected [O III]λ5007 luminosity for Sample B. *Right*: (b) Correlation between the intrinsic X-ray luminosity in the 2–10 keV band and extinction-corrected [O III]λ5007 luminosity for Sample B. The lines are the best-fit regression lines obtained from all (X-ray type-1 and X-ray type-2) AGNs. The symbols are the same as in Figure 1.

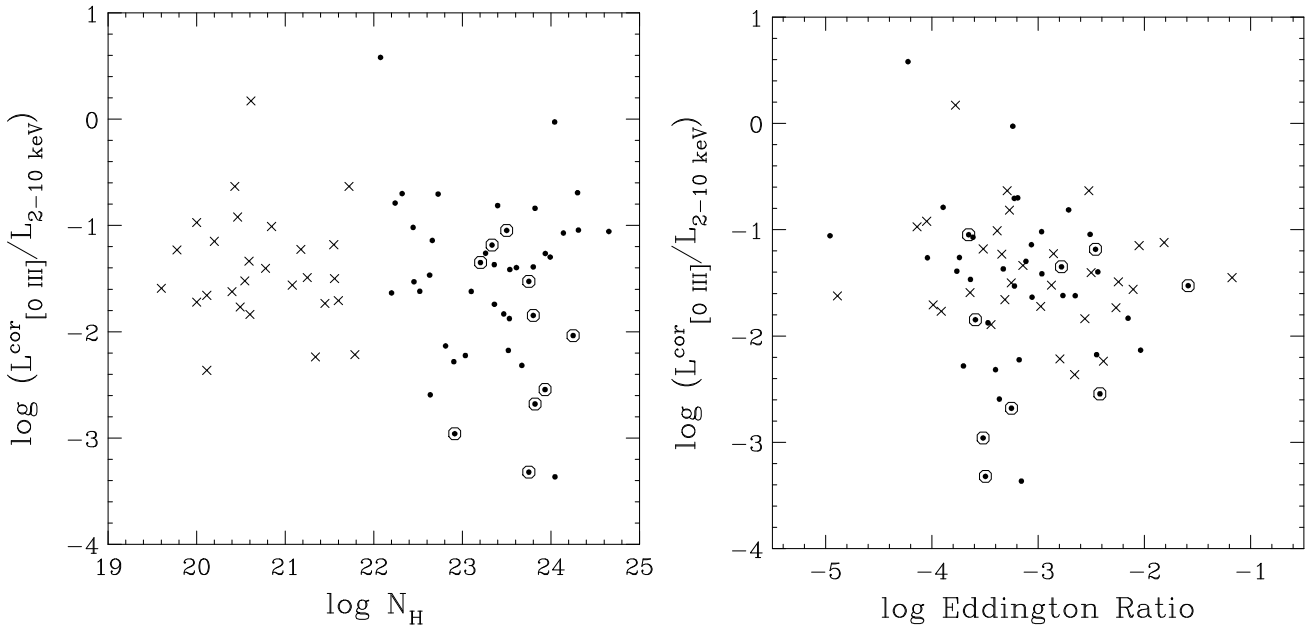

FIG. 4.— *Left*: (a) The ratio of the extinction-corrected [O III]λ5007 luminosity to the intrinsic 2–10 keV luminosity plotted against $N_{\rm H}$ for Sample B. *Right*: (b) The ratio of the extinction-corrected [O III]λ5007 luminosity to the intrinsic 2–10 keV luminosity plotted against X-ray Eddington ratio (the 2–10 keV luminosity normalized by the Eddington luminosity) for Sample B. The symbols are the same as in Figure 1.

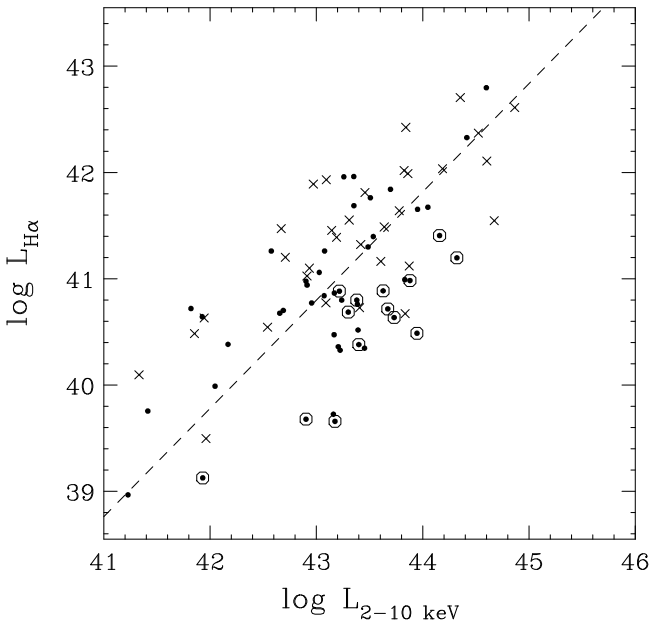

FIG. 5.— Correlation between the intrinsic X-ray luminosity in the 2–10 keV band and Hα luminosity for AGNs in Sample A with available Hα fluxes. The lines are the best-fit regression lines obtained from all (X-ray type-1 and X-ray type-2) AGNs. The symbols are the same as in Figure 1.

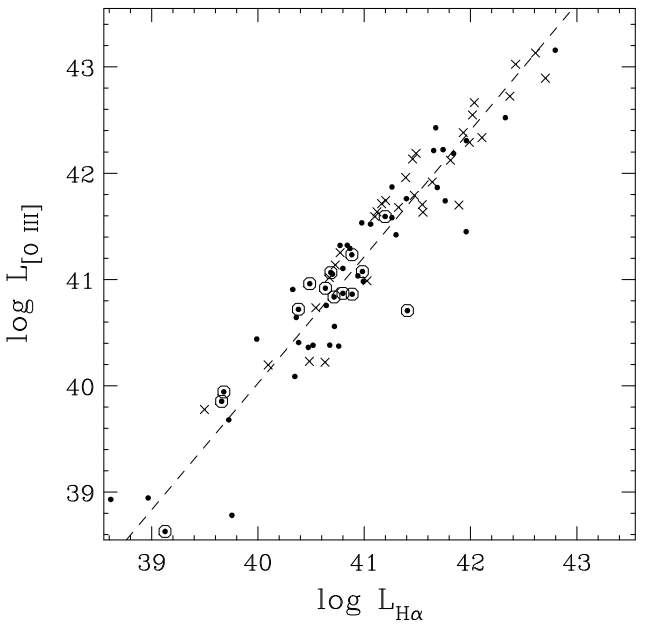

FIG. 6.— Correlation between the Hα luminosity and observed [O III]λ5007 luminosity for AGNs in Sample A with available Hα fluxes. The lines are the best-fit regression lines obtained from all (X-ray type-1 and X-ray type-2) AGNs. The symbols are the same as in Figure 1.

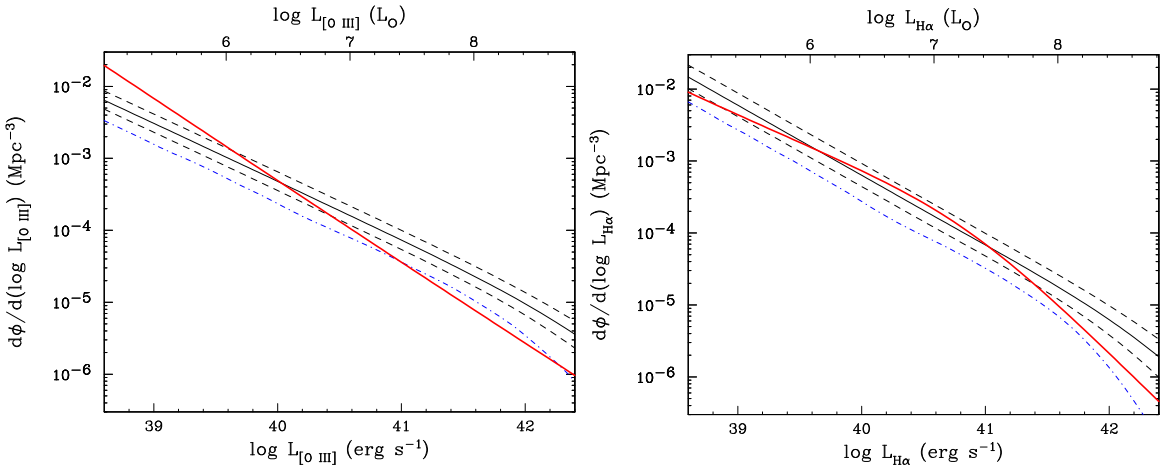

FIG. 7.— *Left*: (a) Comparison of [O III]λ5007 and X-ray luminosity functions (LFs) of local AGNs. The thick solid curve (red) represents the observed [O III]λ5007 LF from the SDSS. The solid curve (black) is a predicted [O III]λ5007 LF from the X-ray LF in the Ueda et al. (2014) model. The region surrounded by the two dashed curves (black) reflects the 1σ uncertainties in the mean and standard deviation in the $\log(L_{[\mathrm{O\ III}]}/L_{2-10})$ ratio. The dot-dashed curve (blue) corresponds to the case with the standard deviation is set to zero. The upper axis gives the [O III]λ5007 luminosities in solar units. *Right*: (b) Same as (a) but for Hα luminosity function.